Room temperature magnetically ordered polar corundum $GaFeO_3$ displaying magnetoelectric coupling

Hongjun Niu[1], Michael J. Pitcher[1], Alex J. Corkett[1], Sanliang Ling[2], Pranab Mandal[1], Marco Zanella[1], Karl Dawson[3], Plamen Stamenov[4], Dmitry Batuk[5], Artem M. Abakumov[5,6], Craig L. Bull[7], Ronald I. Smith[7], Claire A. Murray[8], Sarah J. Day[8], Ben Slater[2], Furio Cora[2], John B. Claridge[1,*] and Matthew J. Rosseinsky[1,*]

[1]Department of Chemistry, University of Liverpool, Crown Street, Liverpool L69 7ZD, UK

[2]Department of Chemistry, University College London, Gower Street, London WC1E 6BT, UK

[3]Centre for Materials and Structures, School of Engineering, University of Liverpool, Liverpool L69 3GH, UK

[4]CRANN, Trinity College Dublin, College Green, Dublin 2, Republic of Ireland

[5]EMAT, University of Antwerp, Groenenborgerlaan 171, 2020 Antwerp, Belgium

[6]Skoltech Center for Electrochemical Energy Storage, Skolkovo Institute of Science and Technology, 143026 Moscow, Russian Federation

[7]ISIS Neutron and Muon Source, Science and Technology Facilities Council, Rutherford Appleton Laboratory, Harwell Oxford, Didcot, Oxfordshire OX11 0QX, UK

[8]Diamond Light Source, Diamond House, Harwell Oxford, Didcot, Oxfordshire OX11 0DE, UK

Abstract

The polar corundum structure type offers a route to new room temperature multiferroic materials, as the partial $LiNbO_3$-type cation ordering that breaks inversion symmetry may be combined with long range magnetic ordering of high spin d^5 cations above room temperature in the $AFeO_3$ system. We report the synthesis of a polar corundum $GaFeO_3$ by a high-pressure high-temperature route and demonstrate that its polarity arises from partial $LiNbO_3$-type cation ordering by complementary use of neutron, X-ray and electron diffraction methods. In-situ neutron diffraction shows that the polar corundum forms directly from $AlFeO_3$-type $GaFeO_3$ under the synthesis conditions. The A^{3+}/Fe^{3+} cations are shown to be more ordered in polar corundum $GaFeO_3$ than in isostructural $ScFeO_3$. This is explained by DFT calculations that

indicate that the extent of ordering is dependent on the configurational entropy available to each system at the very different synthesis temperatures required to form their corundum structures. Polar corundum $GaFeO_3$ exhibits weak ferromagnetism at room temperature that arises from its Fe_2O_3-like magnetic ordering, which persists to a temperature of 408 K. We demonstrate that the polarity and magnetisation are coupled in this system, with a measured linear magnetoelectric coupling coefficient of 0.057 ps/m. Such coupling is a prerequisite for potential applications of polar corundum materials in multiferroic/magnetoelectric devices.

1. Introduction

New low-energy information storage and processing architectures have been proposed which rely on magnetoelectric and multiferroic materials[1-2], but the development of such systems is hampered by a paucity of suitable candidate materials, which must combine magnetic and polar electrical order at (or close to) room temperature. This is challenging because the electronic structure requirements for the two ground states are antagonistic in several respects *e.g.*, classical routes to polar materials rely on the coordination environments of closed shell s^2 and d^0 cations which are not consistent with magnetism[3-5]. The perovskite $BiFeO_3$ partially solves this problem by combining ferroelectrically- and antiferromagnetically-ordered sublattices[6-7]. Several new approaches centred on the ABO_3 perovskite family have emerged recently, such as strain-generated ferromagnetism in epitaxial thin films[8-9], magnetic percolation at morphotropic phase boundary compositions in bulk ceramics[10] and symmetry engineering[11] in bulk[12] and thin film materials[13]. However, the identification of other materials families where the two ground states may co-exist at ambient temperature is less developed. By using the connection between the polar $LiNbO_3$ structure and perovskite, we identified polar derivatives of corundum as a new class of ternary oxide $AFeO_3$ materials that support both magnetic order (from a sufficiently high concentration of Fe^{3+} cations) and electrical order (enabled by cation site ordering), which can be targeted by high pressure synthesis methods[14]. The polar corundum $ScFeO_3$, the first compound of this type, is ordered magnetically above room temperature and the limited extent of long-range cation site order is sufficient to break inversion symmetry, producing electrical polarity (more recently, $LiNbO_3$-type polymorphs of Mn_2FeTaO_6[15] and Zn_2FeTaO_6[16] have been reported with low magnetic ordering temperatures by a similar synthetic approach, and potential ferroelectric switching mechanisms have been investigated computationally[17]). The crystal chemistry of $ScFeO_3$ is complex as, in addition to the

competition between bixbyite and partially ordered corundum phases,[14] higher synthesis pressures stabilise a perovskite phase, from which a fully ordered $LiNbO_3$-type polymorph (with a correspondingly enhanced spontaneous polarisation and Néel temperature) is recovered on decompression[18]. This implies that the structural chemistry of analogous $AFeO_3$ compositions (where *A* is a trivalent cation capable of adopting octahedral coordination) could offer polarity and magnetism if synthesised under appropriate conditions.

The ternary ferrite $GaFeO_3$ represents one such candidate for isolation of a polar corundum phase. While at ambient pressure $ScFeO_3$ adopts the fluorite-derived bixbyite structure with Sc^{3+} and Fe^{3+} coordinated in an edge-sharing network of distorted MO_6 octahedra[19], ambient pressure $GaFeO_3$ adopts the polar orthorhombic $AlFeO_3$ structure with edge-sharing chains of (Ga, Fe)O_6 octahedra and vertex-linked GaO_4 tetrahedra, but only exhibits long-range magnetic ordering and magnetoelectric coupling well below room temperature[20-23]. Like $ScFeO_3$ and $InFeO_3$[24], its structural behaviour at high pressures and temperatures shows complex interplay between corundum and perovskite structures: at ambient temperature, hydrostatic compression to pressures above 40 GPa converts the structure directly to an orthorhombic perovskite, which in turn transforms on decompression to 25 GPa to a corundum-type phase which is retained down to ambient pressure[25]. Corundum-type $GaFeO_3$ can also be obtained directly by annealing at a sufficiently high temperature and pressure[26] and by analogy with $ScFeO_3$ it is possible that a polar variant of this structure will be accessible in this part of the phase diagram. We have targeted and isolated such a polar corundum $GaFeO_3$ phase, demonstrating that a family of materials adopt this structure. Polar corundum $GaFeO_3$ exhibits weak ferromagnetism above room temperature, and the extent of the cation site order is enhanced with respect to that observed in $ScFeO_3$, allowing the measurement of linear magnetoelectric coupling consistent with the polar *R*3*c* space symmetry and the observed α-Fe_2O_3 – like magnetic order.

2. Experimental Details

Synthesis: Initially, the ambient pressure phase of $GaFeO_3$ was prepared from stoichiometric mixtures of Ga_2O_3 (99.999%) and Fe_2O_3 (99.998%) reacted at 900 °C for 12 hours, 1300 °C for 24 hours followed by 1400 °C for 2 hours in an alumina crucible in air. This precursor phase was then annealed under flowing oxygen at 1300 °C for 10 hours, in order to maximise the resistivity of the subsequent high pressure product. The $GaFeO_3$ starting materials were then heated to 150, 500, 700, 900, 1100, 1300 and 1500 °C, respectively, for 10 minutes at 6 GPa

in a Pt-lined alumina crucible encapsulated within a graphite furnace in a Walker-type multi-anvil press. The samples were then cooled to room temperature and the pressure released. The high pressure phase forming at 900 °C was used for structural, electric and magnetic studies.

Powder X-ray diffraction: Phase identification was performed using a PANalytical X'Pert Pro diffractometer in Bragg-Brentano geometry with monochromated Co $K_{\alpha 1}$ radiation (λ = 1.78896 Å). Synchrotron XRD data (SXRD) were collected from the I11 powder diffractometer (Diamond Light Source, UK). The sample was loaded inside a 0.1 mm quartz capillary and data were collected using an incident wavelength λ = 0.827127(1) Å over a 2θ range 2 – 150°, using the high resolution MAC detectors. Anomalous scattering data were collected on beam line I11 from a sample loaded on to the external surface of a 0.3 mm borosilicate capillary. A monochromator scan was used to measure the Ga K edge fluorescence spectrum and an energy of 10.359 keV (λ = 1.196901(5) Å) was selected for the anomalous scattering data set using the high resolution MAC detectors. A corresponding non-anomalous data set was then collected from the same capillary at λ = 0.826185(5) Å.

Powder neutron diffraction: Time-of-flight neutron powder diffraction (NPD) data were collected at ambient temperature and pressure on the POLARIS diffractometer at the ISIS facility, Rutherford Appleton Laboratory (UK). The sample was contained in a quartz capillary of diameter 1.5 mm, filled to a height of 40 mm. The data analysis was performed by Rietveld refinement using Topas Academic (Version 5).

In-situ powder neutron diffraction: High-pressure high-temperature data were collected on the medium-resolution high-flux PEARL diffractometer (ISIS, UK) using a Paris-Edinburgh (PE) press[27]. The sample was pelletised and placed in a high-pressure furnace assembly[28]. The furnace assembly was placed in between WC anvils in a V4 variant PE press dedicated to high temperature pressure measurements. The sample pressure was determined by the equation of state (EoS) of platinum[29]. The temperature was determined by the resonance technique from the Hf foils included in the sample volume[30]. Time of flight data were collected using the 90 degree detector bank over a d-spacing range of 0.5-4 Å and corrected for anvil attenuation using in-house routines[27]. The hydraulic load of the press was gradually increased until the desired sample pressure was achieved prior to heating. The data analysis was performed by Rietveld refinement using Topas Academic (Version 5).

SQUID Magnetometry: Magnetic measurements were carried out on powder samples using a commercial superconducting quantum interference device (SQUID) magnetometer MPMS XL – 7 and MPMS3 (Quantum Design, USA). Magnetization vs. temperature data were recorded from 5 K to 900 K in the following modes: ZFC (zero-field cooling), FC (field cooling) and

TRM (thermoremanent magnetization). The magnetic field-dependent magnetization was also measured at 10, 200, 400 and 420 K between -9 kOe and 9 kOe.

Magnetoelectric coupling: For magnetoelectric (ME) measurements, the polar corundum sample was polished to a 5 micron finish using SiC paper in a semi-automatic polishing machine. Ohmic contacts were made via sputtering Pt. ME measurements were carried out on a modified SQUID magnetometer[31]. Prior to the measurements the sample was poled in the following sequence: slowly cooled (1 - 2 K/min) from 350 K to 130 K in a 20 kOe magnetic field and zero electric field (short circuit). At 100 K, an electric field of 350 – 400 kV/m was applied while cooling down in the same magnetic field to the measurement temperature at 1 K/min. After poling, electric and magnetic fields were switched off and electrodes were short circuited for 15 minutes.

Dielectric constant Dielectric properties were measured using an Agilent 4980 precision LCR meter for frequencies of 20 Hz to 2 MHz in the temperature range of 30−500 °C. A ramp rate of 1 °C min^{-1} was used. The sample with sputter coated Pt electrodes on both sides was loaded in a home-made sample holder and data were collected using the LABVIEW program.

Differential Scanning Calorimetry (DSC): Heat flow was measured from a powder sample in an aluminium pan between room temperature to 500 °C by the modulated DSC technique using a DSC Q2000 instrument (TA Instruments).

In-situ resistance: Two-probe dc electrical resistance measurements as a function of temperature at 6 GPa were carried out using Keithley 220 programmable current source and Keithley 2182 Nanovoltmeter. The $GaFeO_3$ powder was loaded into the alumina crucible and Pt plates were employed on both the top and bottom of the crucible as the electrodes.

ICP-OES measurements: Powder samples of $GaFeO_3$ (approximately 50 mg) were dissolved in 10 cm^3 HF-HCl mixture (UniSolv Acid Dissolution Reagent 1, Inorganic Ventures) with 10 drops of concentrated HNO_3. The solution was then neutralised with 50 cm^3 of triethanolamine-triethylenetretramine solution (UNS-1 solution, Inorganic Ventures) and diluted to approximately 20 ppm. The same protocol was used to prepare a standard solution from a stoichiometric mixture of Ga_2O_3 and Fe_2O_3. Measurements were collected on a Spectro Ciros Vision ICP-OES instrument.

TEM-EDX: EDX measurements were performed on a Jeol 2000FX using an EDAX EDX detector. Sample powder was dispersed in 500µl of ethanol and a drop of the suspension was dropped on a carbon coated TEM copper grid. EDX spectra were collected for several minutes in order to obtain a suitable signal to noise ratio. Compositions were calculated from the mean of 25 particles.

Convergent beam electron diffraction (CBED): Specimens were prepared using a FEI Helios 600i focussed (Ga) ion beam instrument. Thin lamellae were sectioned and mounted on Cu grids using the lift out technique. Primary milling was performed using an acceleration voltage of 30kV, final cleaning passes were applied to specimen surfaces using a low energy (5kV) polish. CBED experiments were performed in JEOL 2000FX microscope operated at 200keV.

SAED and HAADF-STEM: TEM specimens were prepared by grinding the powder sample under ethanol and depositing several drops of the dispersion onto holey carbon grids. The selected area electron diffraction (SAED) patterns were recorded using a Tecnai G2 microscope operated at 200 kV. The Fe and Ga distribution in the structure was investigated using high angle annular dark field scanning TEM (HAADF-STEM) imaging. The experiment was conducted on a probe aberration-corrected Titan 80-300 microscope operated at 300 kV. Theoretical HAADF-STEM images have been calculated using the QSTEM 2.20 software.

Mossbauer spectroscopy: Mössbauer spectroscopy was performed in absorption, at room temperature, using a WissEl (MA-260) electromagnetic Doppler drive system, a 57Co(Rh) gamma source, of actual activity of ~40 mCi and Xe-gas Reuter-Stokes proportional counter. Canberra amplification, discrimination and scaling electronics were used to acquire sample and α-Fe calibration spectra of width of 512 channels, to a level of approximately 10^7 counts per channel. Samples were diluted with sucrose (icing sugar) for measurements at an approximate ratio of 0.2, in order to prevent excessive line-shape distortion and non-resonant absorption. Custom folding, absorber geometry modelling and non-linear least squares regression routines were used for the extraction of the spectroscopic parameters and their errors. Isomer shifts are referred to the source.

Computational: All calculations were performed under periodic boundary conditions, using the CP2K[32-33] code which employs a mixed Gaussian/plane-wave basis set. We employed double-ζ polarization quality Gaussian basis sets[34] and a 600 Ry plane-wave cutoff for the auxiliary grid, in conjunction with Goedecker−Teter−Hutter pseudopotentials[35-36]. Total energy calculations and structural optimizations, including both atomic coordinates and cell parameters, were performed at the hybrid density functional theory (DFT) level using the PBE0 exchange and correlation functional[37-38], which has 25% Hartree-Fock exchange (HFX). The HFX calculations were significantly accelerated by using the auxiliary density matrix method (ADMM)[39] and a truncated potential[40], with which the HFX energy becomes zero beyond a pre-defined real-space cutoff radius. For production quality calculations we have used the cpFIT3 auxiliary basis sets and a cutoff radius of 4 Å, a convergence threshold of 5.0×10^{-6}

Ha for the self-consistent field cycle, and structural optimizations were considered to have converged when the maximum force on all atoms falls below 4.5×10^{-4} Ha $Bohr^{-1}$. Calculations were performed with the Γ-point approximation using a $2 \times 2 \times 1$ multiplication of the hexagonal primitive cell consisting of 120 atoms. Additional calculations in a $3 \times 3 \times 1$ supercell (270 atoms) show that the relative energy between FM and AFM magnetic configurations in the $LiNbO_3$ cation order converged to within 5 meV/f.u. in the $2 \times 2 \times 1$ supercell. A comprehensive and systematic configurational and compositional search on $ScFeO_3$ and $GaFeO_3$ in the corundum structure was performed as part of this study (described fully in the Supporting Information), in which the $LiNbO_3$ structure was identified as the ground state of corundum-type $ScFeO_3$. The ground state of corundum-type $GaFeO_3$ was found to be phase separated layers of Fe_2O_3 and Ga_2O_3, hence discussion of phase stability refers to $LiNbO_3$ and "phase separated" as the ground state references for $ScFeO_3$ and $GaFeO_3$ respectively. Additional details of the computational study, including defect formation energies, configurational search, and estimation of configurational entropies, are provided in the Supporting Information (including Figures S1 – S3, and Tables S1 – S2).

3. Results

3.1. Isolation and stability of corundum $GaFeO_3$

Extensive investigation of (T, P) synthesis conditions in the multianvil cell revealed a 700-900°C temperature range at 6 GPa that afforded a diffraction pattern that could be indexed solely with a corundum unit cell after decompression and cooling to room temperature (Figure 1a). The composition was confirmed to be stoichiometric $GaFeO_3$ by ICP-OES measurements (Table S3), with a high level of compositional homogeneity confirmed by TEM-EDX (Figure S4). Reaction at higher temperatures produces Fe_3O_4 as a secondary phase in increasing quantity (2 wt.% 1100°C, 19 wt.% 1500°C) while 500 °C affords partial conversion of ambient pressure $GaFeO_3$ to the corundum structure. In-situ neutron diffraction data collected at 4.7 GPa confirms that the ambient pressure orthorhombic $GaFeO_3$ is converted directly to a corundum-type phase (Figure 1b, c). Higher resolution information on the transformation temperature is provided by in-situ measurement of dc resistance under the synthesis conditions: by cycling a sample to increasing maximum temperatures, its resistance was found to decrease irreversibly during cycles to 400 and 550 °C signifying the onset of the phase transformation, before returning to near-reversible behaviour for cycles to 650 and 800 °C, consistent with

completed formation of the corundum phase (Figure 1d). A second sample was cycled four times between ~25 – 900 °C and showed an irreversible decrease in resistance on the first cycle, which coincides with the resistivity of subsequent cycles at 550 °C (Figure S5), implying that complete conversion to the corundum is achieved at this temperature. This is consistent with both the ex-situ PXRD where the pattern is already dominated by the corundum phase at 500 °C, and the in-situ NPD where the refined $AlFeO_3$-phase content reaches a minimum plateau at 575 °C.

To better understand the isolation of polar corundum $GaFeO_3$ under high pressure reaction conditions, we calculated the enthalpies of different polymorphs of $GaFeO_3$ at different pressures up to 40 GPa. We considered the ambient pressure $AlFeO_3$-type structure, an orthorhombic perovskite structure, the $LiNbO_3$ and ilmenite ordered corundum structures, and the ground state corundum configuration produced by our configurational search (in which Ga and Fe form a structure with distinct [001] blocks at either end of the corundum cell, see Supporting Information and Figure S1). Their enthalpies were compared with those of the binary oxides using the ambient pressure forms α-Fe_2O_3 and β-Ga_2O_3 as the references. Finally, an estimate of the configurational entropies available to the $AlFeO_3$- and $LiNbO_3$-type structures was calculated at 1200 K (see Supplementary Text). The calculated entropies as a function of pressure are plotted in Figure 2a, with the estimated entropic contribution to the total energy at 1200 K overlaid for these two structure types to illustrate the estimated extent of entropic stabilization. The equivalent calculations for the same polymorphs of $ScFeO_3$, using α-Fe_2O_3 and bixbyite-type Sc_2O_3 as the references, are shown in Figure 2b.

For $GaFeO_3$, the ambient pressure $AlFeO_3$ structure is the most stable ternary phase at 0 GPa, and is stable relative to the binaries when configurational entropy of 98.8 meV/f.u. at 1200 K is considered. At this pressure, the $LiNbO_3$ structure is unstable with respect to its binary constituents by 159 meV/f.u at 0 K. With increasing pressure, the $AlFeO_3$ structure is progressively destabilised, and the corundum-type structures become the most stable beyond ~3 GPa. Among the corundum-type structures, the $LiNbO_3$ cation ordering is found to be more stable than the ilmenite ordering at all pressures. At ~30 GPa the perovskite structure becomes more stable than the $LiNbO_3$ structure, which is in good agreement with experimental work[25]. In $ScFeO_3$, the $LiNbO_3$ structure is the most stable ternary phase at 0 GPa but is less stable than the binary mixture by 128 meV/f.u; the orthorhombic perovskite phase is stabilised more rapidly with pressure and becomes the most enthalpically stable phase at ~7 GPa.

These results show that configurational entropy due to disorder of Ga and Fe cations in the $AlFeO_3$ and corundum lattices at the synthesis temperatures plays a critical role in the stabilisation of the ternary phases. This is consistent with our configurational search of corundum-type $GaFeO_3$ (see Figure 3a), where a total of 151 configurations, including the fully ordered $LiNbO_3$ structure, are found within 50 meV/f.u. (~0.5 kT at the synthesis temperature of 1200 K) of the lowest energy configuration: these may correspond to states that are accessible under the synthesis temperature. This contrasts with $ScFeO_3$, which has only 5 configurations within 50 meV/f.u. of the fully ordered $LiNbO_3$ ground state (Figure 3b), indicating that a higher temperature is required to entropically stabilise the corundum structure of $ScFeO_3$ by accessing a greater number of configurations.

3.2. Structural analysis

The synchrotron powder X-ray diffraction (SXRD) patterns of $GaFeO_3$ synthesised at high pressure could be indexed to an *R*-centered hexagonal unit cell with lattice parameters a = 5.01936(4) Å, c = 13.5903(1) Å), as shown in Figure 4a, which is consistent with the corundum structure adopted by α-Fe_2O_3[41-42]. The observed reflection conditions (*h*-*h*0*l*: *h*+*l* = 3n, *l* = 2n), also observed in selected area electron diffraction (SAED) patterns (Figure 4c), are consistent with *R*3*c* and $R\bar{3}c$ space groups which correspond to the polar $LiNbO_3$ and non-polar (fully disordered) corundum structures respectively. These systematic absences preclude the possibility of an ilmenite structure type with $R\bar{3}$ space symmetry. Regarding the possible acentric *R*3*c* and centrosymmetric $R\bar{3}c$ structural models of $GaFeO_3$, the very similar X-ray scattering factors of Fe^{3+} and Ga^{3+} preclude unambiguous space group assignment from Rietveld refinement against PXRD data alone. We addressed this problem in two parts: firstly, by using convergent beam electron diffraction (CBED) to determine the point group of the $GaFeO_3$ corundum; and secondly by employing powder neutron diffraction and anomalous X-ray scattering to determine the extent of the cation ordering.

The whole pattern symmetry of the [$5\bar{5}1$] zone from CBED (Figure 4b) displays only a single *m* symmetry element. Considering only trigonal crystal systems this permits the assignment of the 3*m* point group[43] and along with the observed reflection conditions from PXRD data indicates that the high pressure phase of $GaFeO_3$ crystallises in the non-centrosymmetric *R*3*c* space group. To confirm the assignment of the *R*3*c* space group and investigate the degree of cation order in $GaFeO_3$, neutron powder diffraction (NPD) analysis of two samples synthesised by the same protocol utilized the modest contrast in the neutron scattering lengths of Fe (9.45

fm) and Ga (7.288 fm). The appearance of Bragg peaks that were not present in the SXRD pattern, including two intense reflections at 4.14 and 4.54 Å, confirmed the presence of long range magnetic order at room temperature. The magnetic structure was determined by representational analysis using the SARAh package[44] and found to be a k = 0 G-type antiferromagnetic arrangement analogous to the high temperature antiferromagnetic structure of α-Fe_2O_3[45] with spins aligned parallel to the a axis. Structural models in $R3c$ ($LiNbO_3$) and $R\bar{3}c$ (corundum) were refined against four Polaris data banks simultaneously, with the magnetic structure modelled in a $P1$ cell. In the disordered corundum ($R\bar{3}c$) refinement, the magnitudes of the magnetic moments were constrained to a single refined value to reflect the statistical distribution of Fe^{3+} cations. In the cation-ordered model ($R3c$), the occupancies of Ga^{3+} and Fe^{3+} on each site in the nuclear phase were refined with a constraint on the total composition, and the magnetic phases were modelled with two independently refined moments, whose positions in the $P1$ cell corresponded to the $LiNbO_3$-type cation ordering. In addition to site occupancy refinement in the $LiNbO_3$ model, atomic coordinates and isotropic thermal displacement parameters (B_{iso}) were refined with B_{iso} constrained to be equal for the Fe/Ga sites.

For both samples the best goodness of fit was obtained from refinement in the $R3c$ space group, with $R\bar{3}c$ (disordered corundum) giving the higher χ^2 (see Tables S4 and S5). Inspection of the refined $R3c$ model revealed that the refined cation occupancies from the nuclear scattering in $R3c$ resulted in compositions of $[Ga_{0.68(2)}Fe_{0.32(2)}][Ga_{0.32(2)}Fe_{0.68(2)}]O_3$ (36(2) % ordered, defined by the difference in site occupancy) and $[Ga_{0.62(3)}Fe_{0.38(3)}][Ga_{0.38(3)}Fe_{0.62(3)}]O_3$ (24(3)% ordered) for the two samples, which is consistent with the relative magnitudes of the ordered spins on each site in the magnetic structure: the ordered moment at the Fe-rich site in sample 1 refined to 2.15(2) μ_B, whilst that of the Fe-poor site refined to 1.03(3) μ_B. Assuming that individual Fe have the same moment at each site, then the refined (average) moments are due to different populations of Fe at each site, which yields $[Ga_{0.68(1)}Fe_{0.32(1)}][Ga_{0.32(1)}Fe_{0.68(1)}]O_3$, and the equivalent calculation for sample 2 yields $[Ga_{0.65(1)}Fe_{0.35(1)}][Ga_{0.35(1)}Fe_{0.65(1)}]O_3$). The Rietveld fits are shown together with the refined $R3c$ model in Figure 5. The consistency between the extent of cation ordering obtained directly from the nuclear scattering, and the extent of ordering obtained independently from the magnetic scattering, in addition to the superior goodness of fit, confirms the assignment of polar $R3c$ symmetry. The polarization of $GaFeO_3$ was calculated as 6.9 $\mu C.cm^{-2}$ from a formal point charge model, using the program PSEUDO[46] with the refined atomic coordinates of sample 1.

Anomalous scattering synchrotron X-ray diffraction at the Ga K edge provides an alternative probe of the extent of cation order. The *R*3*c* model was refined simultaneously against two histograms, collected at ambient temperature at resonant (10.359 keV) and non-resonant (15.119 keV) energies from sample 1. The background was fitted by refinement of a Chebyschev polynomial function, and peak profiles were modelled by a Pearson VII function with a refined axial divergence correction. Lattice parameters, atomic coordinates and isotropic thermal displacement parameters were refined independently for each site, and a Suortti surface roughness (absorption) correction was refined for each histogram. Initially a series of $[Ga_xFe_{1-x}][Ga_{1-x}Fe_x]O_3$ models with the extent of cation ordering (x) varied systematically between $0 \leq x \leq 1$ were refined, and the resulting plot of χ^2 *vs* x (Figure S6) showed two shallow minima centred approximately at x = 0.4 and x = 0.6, consistent with the partial cation ordering observed by NPD. By allowing x to refine freely, a composition $[Ga_{0.596(4)}Fe_{0.404(4)}][Ga_{0.404(4)}Fe_{0.596(4)}]O_3$, which is 19.2(6)% ordered, was obtained which is within four standard deviations of the NPD value (furthermore, the shallow minima in χ^2 vs x indicate that the reported least squares errors on x from SXRD are underestimated). Both the NPD and SXRD results are also consistent with the computational screening of configurational entropy; the average cation order in the 2331 configurations examined and displayed in Figure 3, weighted by their relative population at 900 °C, yields a value of $[Ga_{0.61}Fe_{0.39}][Ga_{0.39}Fe_{0.61}]O_3$.

HAADF-STEM was used as a local probe to image the cation ordering directly. The two crystallographic positions jointly occupied by Fe and Ga form separate atomic columns in the structure as viewed along the $[24\bar{6}1]$ (= $<100>_p$) direction (Figure S7). In HAADF-STEM, the observed intensity is proportional to the composition of the atomic columns and scales approximately as $Z^{1.6\text{-}1.9}$ (where Z is the average atomic number of the projected columns). Because of a very small difference between the average Z of the Fe-rich and Ga-rich atomic columns (Z = 27.6 and 29.4, respectively), the associated difference in brightness is expected to be subtle (see the calculated intensity profile in Figure 6c). Nevertheless, the intensity profiles taken from the experimental $[24\bar{6}1]$ HAADF-STEM image (Figure 6a, b) show systematic intensity differences reminiscent of that observed on the profile from the calculated image (Figure 6c). All of these structural analyses confirm the *R*3*c* space group with partial Ga/Fe order in the polar corundum structure.

3.3. Magnetic order and magnetoelectric coupling

Mössbauer spectroscopy of polar corundum $GaFeO_3$ at ambient temperature and pressure confirms the long range magnetic order demonstrated at room temperature by neutron diffraction (Figure 7d, with fitted parameters shown in Table 3). The absorption pattern is clearly decomposed into a combination of two magnetically-ordered sites, with average hyperfine fields of 39.48 T and 33.09 T, respectively (the larger of the two being close to that of Goethite[47] with its transition temperature of ~400 K[48]) which account for 91.09(2) % of the fitted area, with the remainder assigned to one asymmetric paramagnetic doublet accounting for 8.91(2) % of the fitted area, which is a dynamic line shape resulting from the proximity of the Néel temperature. The two main sites exhibit significant static hyperfine field distributions of width of 0.2 – 0.3 T. The fitted isomer shift (IS) of 0.25 mm/s and quadrupole splitting of 0.19 mm/s are consistent with Fe^{3+}, but the IS is smaller than expected for a typical octahedral coordination in an oxide, which may be due to the high degree of static disorder in the system. Isomer shifts of <0.25 mm/s have been reported under applied hydrostatic pressure for a corundum $GaFeO_3$ produced by transformation from the metastable perovskite (and thus likely to be highly ordered)[25], demonstrating a high degree of sensitivity of IS to local coordination environment in this system.

Figure 7a shows the magnetisation of polar corundum $GaFeO_3$ measured in an applied magnetic field of 1000 Oe in zero field cooled (ZFC), field cooled (FC) and thermoremanent magnetisation (TRM) from 300 K to 500 K. ZFC/FC divergence appears at 408 K together with the onset of TRM. The M(H) isotherms in Figure 7b are consistent with this magnetic ordering temperature of 408 K. The linear isotherm at 420K shows that the sample is paramagnetic, with hysteresis observed at and below 400K, consistent with weak ferromagnetism occurring simultaneously with the antiferromagnetic order. ZFC, FC and TRM magnetisation data between 5 and 350 K (Figure S8), show that no magnetic transition occurs below 408K. The remanent magnetisation was 0.012 μ_B/f.u. at 10 K (Figure 7b).

In order to minimise spurious signals caused by leakage currents**,** magnetoelectric measurements were carried out at 10 K on the polar corundum $GaFeO_3$ sample poled both electrically and magnetically (the resistivity at 10 K, measured in-situ, was 2.38 x 10^{12} Ω.m). The ME susceptibility (α), measured as the slope of the induced ac magnetization (M_{ac}) versus the applied ac electric field amplitude (E_{ac}) is 0.057 ps/m. (Figure 7c). The observation of linear magnetoelectric coupling is consistent with the symmetry of the magnetic structure: above the

Morin transition,[45] α-Fe_2O_3 adopts *2/m* magnetic point symmetry (which is centrosymmetric, permitting weak ferromagnetism but not linear magnetoelectric coupling[49]), but the cation ordering in polar corundum $GaFeO_3$ eliminates the inversion centre, thus lowering the magnetic point symmetry to *m*,[50] which permits both weak ferromagnetism and linear magnetoelectric coupling[49]. The observed magnitude of α is similar to that observed in other Fe-based polar magnetoelectrics that are ordered magnetically above room temperature.[10, 12, 51] Attempts to measure electrical polarization loops were hampered by the high dielectric loss at room temperature, whilst measurements at 100 K were possible at applied fields of up to 120 $kVcm^{-1}$ but did not achieve ferroelectric switching.

3.4. Thermal stability

To test the thermal stability and decomposition behaviour of polar corundum $GaFeO_3$ at ambient pressure, the as-made samples were annealed at different temperatures between 300 – 1000 °C in air. Ex-situ PXRD patterns of the post-annealed samples showed that the orthorhombic ambient pressure phase is recovered after annealing at 1000 °C, but the corundum unit cell is retained after annealing at 300 – 800 °C with no apparent decomposition (Figure S9). However, DSC (Figure 9) and in-situ dielectric measurements (Figure 10) collected on heating from 25 – 500 °C show an endothermic peak, and a corresponding peak in the dielectric constant, which is frequency-independent (Figure S10) and centred at approximately 200 °C. The feature is strongly pronounced during the first heating cycle and absent in subsequent cycles, which indicates the occurrence of an irreversible phase transition. To investigate whether this is associated with a loss of polarity in the sample, CBED images, magnetisation and magnetoelectric coupling data were collected on annealed samples.

Figure 7c shows the ME susceptibility α decreases from 0.057 ps/m for as-made polar corundum $GaFeO_3$ to 0.003 ps/m for the sample annealed at 380 °C: for this sample, the induced magnetic moment is below the detection limit of 10^{-9} emu. Close inspection of the CBED whole pattern symmetry for the $[\bar{1}11]$ zone axis (Figure S11) reveals the sample to have retained 3*m* point symmetry, which implies that the sample has retained some residual polarity. Taken together with the magnetoelectric measurements, this implies that the polarity of the material (via the cation ordering) is diminished, but not eliminated entirely, by annealing polar corundum $GaFeO_3$ at this temperature. The weak ferromagnetism, which arises from the α-

Fe_2O_3-type magnetic structure, is also retained after thermal treatment (Figure S12). This is consistent with the *2/m* magnetic point symmetry of α-Fe_2O_3 above the Morin transition[45]: the loss of cation ordering in polar corundum $GaFeO_3$ would restore the inversion centre, thus raising the magnetic point symmetry back to 2/*m* (which is centrosymmetric, permitting weak ferromagnetism but not linear magnetoelectric coupling[49]).

4. **Discussion**

Under the high temperature, high pressure conditions applied in this study, a corundum phase of $GaFeO_3$ forms directly from the ambient pressure phase, in contrast to the sequence of phases observed on application of pressure at room temperature where a corundum phase is accessed via a non-quenchable perovskite phase[25]. The fact that the phase does not form by transformation from the high pressure perovskite phase[18, 25] means that the extent of Ga/Fe ordering is limited, producing the polar corundum structure rather than the fully ordered $LiNbO_3$ structure. NPD and X-ray anomalous scattering experiments demonstrate a greater degree of ordering in $GaFeO_3$ than in the isostructural $ScFeO_3$. Our computational results imply that $GaFeO_3$ should have a greater tendency towards cation disorder than $ScFeO_3$ at a given synthesis temperature, as demonstrated by the higher number of accessible cation configurations in $GaFeO_3$ (Figure 3). This originates from the small overall energy cost of Ga/Fe site swaps in $GaFeO_3$, while only the antisite Sc/Fe defect within face-shared dimers is energetically possible in $ScFeO_3$. While the enthalpy of the polar corundum phase of both $GaFeO_3$ and $ScFeO_3$ is unstable relative to the binary oxides, the higher entropic content of $GaFeO_3$ (provided by the large number of thermally accessible cation configurations in the corundum cell at the synthesis temperature) means that its polar corundum phase is stabilised at lower temperature than that of $ScFeO_3$. Experimentally, this results in polar corundum $GaFeO_3$ being stabilized at 900 °C, while polar corundum $ScFeO_3$ must be synthesized at a much higher temperature of 1400 °C. The effect of the different synthesis temperatures of the two materials is expected to have an impact on the extent of cation ordering. From our previous Monte Carlo simulation of $ScFeO_3$[14], it was clear that between 1300 and 1450 K, $ScFeO_3$ transformed from a mainly ordered to a mainly disordered structure: it is also clear that $ScFeO_3$ is calculated to be much more ordered than $GaFeO_3$ at 1200 K, with a site occupancy of ~0.9. This indicates that the experimentally observed cation disorder in polar corundum $ScFeO_3$ is driven by the enhanced configurational entropy at the higher synthesis temperature. In $GaFeO_3$, the low synthesis temperature of 900 °C provides sufficient configurational entropy to stabilise the polar corundum, but it is insufficient to disorder the material to the same extent as seen for

$ScFeO_3$ synthesised at 1400 °C, and consequently produces more ordered compounds. We note the creation of anti-site defects in $LiNbO_3$-type $GaFeO_3$ (*e.g.* by swapping cations in adjacent face-sharing MO_6 octahedra, as described in Supporting Information) is less energetically demanding than in $LiNbO_3$-type $ScFeO_3$, see Table S2, and the anti-site defects may be partly responsible for the cation disorder in polar corundum $GaFeO_3$. It is possible that another source of disorder could originate from the precursor of corundum $GaFeO_3$, *i.e.* the ambient pressure $AlFeO_3$-type, in which extent of cation ordering is dependent on the synthesis conditions[52] and predicted from our simulation based on small energy costs of creating anti-site defects (see Table S6 in the Supporting Information). This implies that a more ordered polar corundum $GaFeO_3$ may be obtained from a highly ordered precursor, *e.g.* the fully ordered perovskite, as observed experimentally in $ScFeO_3$[18].

In most respects the refined crystal structure of $GaFeO_3$ is very similar to that of $ScFeO_3$. The unit cell volume of $GaFeO_3$ is approximately 10 % smaller than that of $ScFeO_3$ on account of the smaller ionic radius of Ga^{3+} (0.62 Å) versus Sc^{3+} (0.745 Å). This is an isotropic contraction driven by the smaller average size of the MO_6 coordination octahedra, as indicated by the similar *c/a* ratios in the two compounds (2.71 and 2.69, respectively). The unit cell dimensions of $GaFeO_3$ are very close to those of α-Fe_2O_3[41-42] and are consistent with those reported from corundum structured $GaFeO_3$ in a recent in-situ high pressure study[25]. The refined metal-oxide distances, illustrated in Figure 5, lie in the range 1.93 – 2.13 Å, and the refined volume of the Ga-rich MO_6 polyhedra (10.49 $Å^3$) are slightly smaller than those of the Fe-rich polyhedra (10.64 $Å^3$), consistent with the relative ionic radii. As in the binary corundums and $ScFeO_3$, the cations are displaced from the centres of the face-sharing MO_6 octahedra by electrostatic repulsion.

Polar corundum $GaFeO_3$ exhibits weak ferromagnetism with an ordering temperature of 408 K; this is approximately 50 K higher than the ordering temperature observed in $ScFeO_3$[14], which may be due to its enhanced cation ordering. The remanent magnetisation of $GaFeO_3$ (0.012 μ_B / f.u.) is comparable to that observed in $ScFeO_3$ (0.0106 μ_B / f.u.)[14]. The combination of weak ferromagnetism and absence of inversion symmetry permits magnetoelectric coupling in $GaFeO_3$. The observed linear magnetoelectric susceptibility (α) of 0.057 ps m^{-1} is small in comparison to other Fe-based polar weak ferromagnetic ceramics[10, 51], but the fact that the room temperature structure is identical to the structure at the measurement temperature (10 K) implies that, given definition of a suitable processing protocol, magnetoelectric coupling may be attainable under ambient conditions in this compound. The magnitude of this coupling falls

below a detectable value when the sample is heated to 380 °C at ambient pressure. DSC and dielectric measurements suggest that this is due to an irreversible phase transition, CBED patterns however indicate that 3*m* point symmetry is still present in the sample. This indicates that the polarity of the sample (driven by the cation ordering that defines the polar corundum structure type) is degraded sufficiently to weaken the ME response below the detection limit, but is not entirely eliminated by annealing under these conditions. Ultimately, the ambient pressure phase is recovered by annealing at a sufficiently high temperature.

5. Conclusions

$GaFeO_3$ is the second member of the polar corundum family, and the first to display ME coupling. The enhanced cation site order in $GaFeO_3$ over $ScFeO_3$ confirms the distinction of this family both from non-polar corundum and from fully $LiNbO_3$-ordered derivatives: the less extreme synthesis conditions required to access polar corundum indicate that a broad family of materials should be accessible, for example through multiple cation decoration of corundum.

The magnetoelectric coupling shows that the engineered co-existence of magnetisation and polarisation in new structural families is a route to coupling these degrees of freedom – thin film growth, already achieved for $ScFeO_3$[14], is a route to tune this further. The relationship between M, α and the cation site order is also controllable via site-ordering extent. The absence of measurable magnetic impurities under the optimised synthesis conditions is consistent with the stability and chemical robustness of this new family of room temperature polar magnetic magnetoelectric materials.

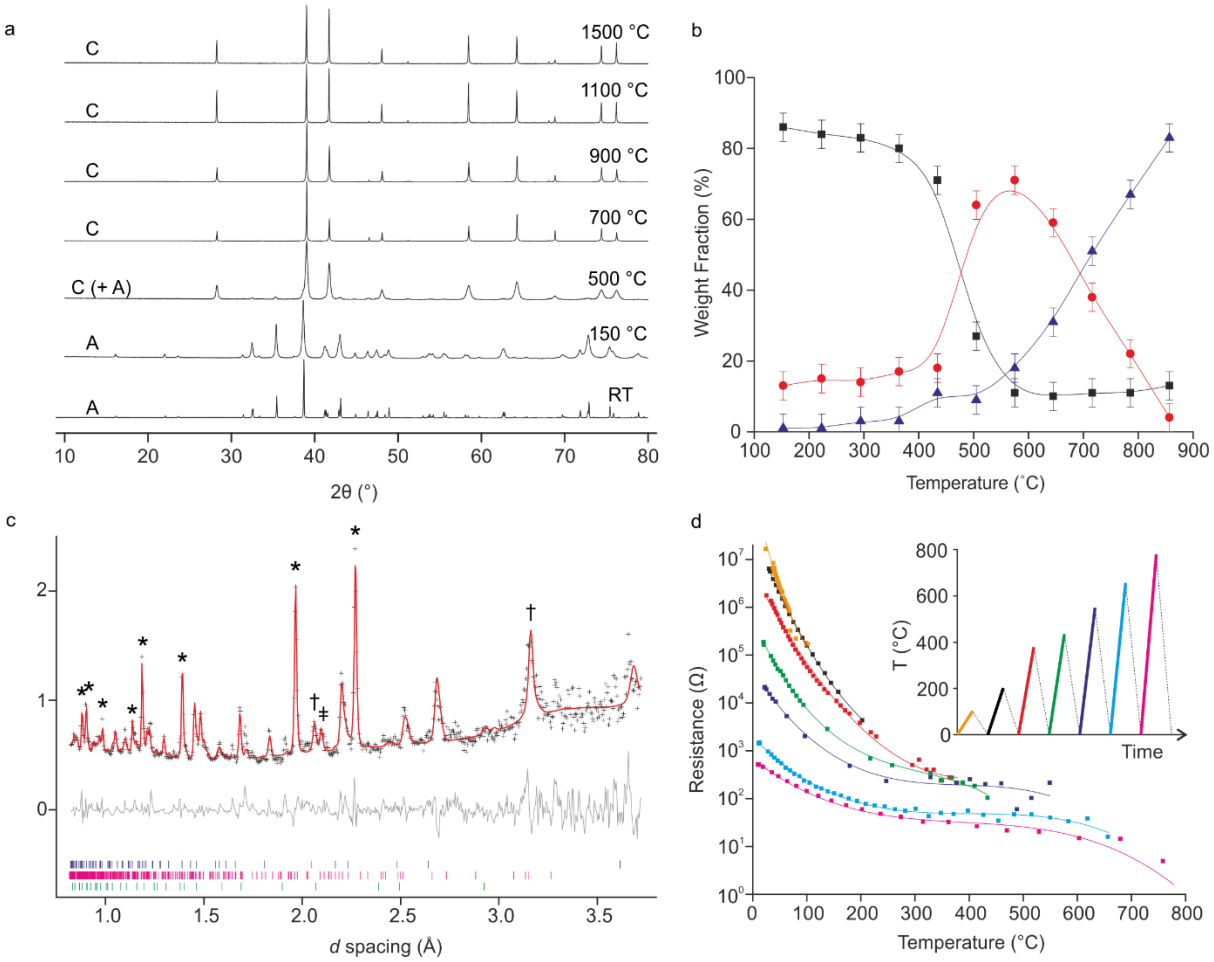

Figure 1: Formation of the corundum phase by high temperature high pressure annealing. (a) Laboratory PXRD patterns obtained from $GaFeO_3$ quenched from a range of temperatures after annealing at 6 GPa. Patterns labelled A contain the starting $AlFeO_3$-structured phase, and those labelled C contain the corundum phase. (b) Refined weight fraction of the $AlFeO_3$ (black), corundum (red) phases and spinel decomposition phase (blue) as a function of temperature at 6 GPa from in-situ neutron diffraction. (c) Rietveld refinement against in-situ neutron data collected at 6 GPa, 500 °C. Blue tick marks = corundum phase, magenta = $AlFeO_3$ phase, green = spinel phase. Asterisks (*) mark peaks from the Pt pressure calibrant; daggers (†) mark graphite peaks, double dagger (‡) marks a vanadium peak. (d) In-situ resistance measurements collected from a pellet of $GaFeO_3$ at 6 GPa cycled to increasing temperatures. Lines are a guide to the eye. The colours of the points correspond to their position in the heating sequence, which is shown inset.

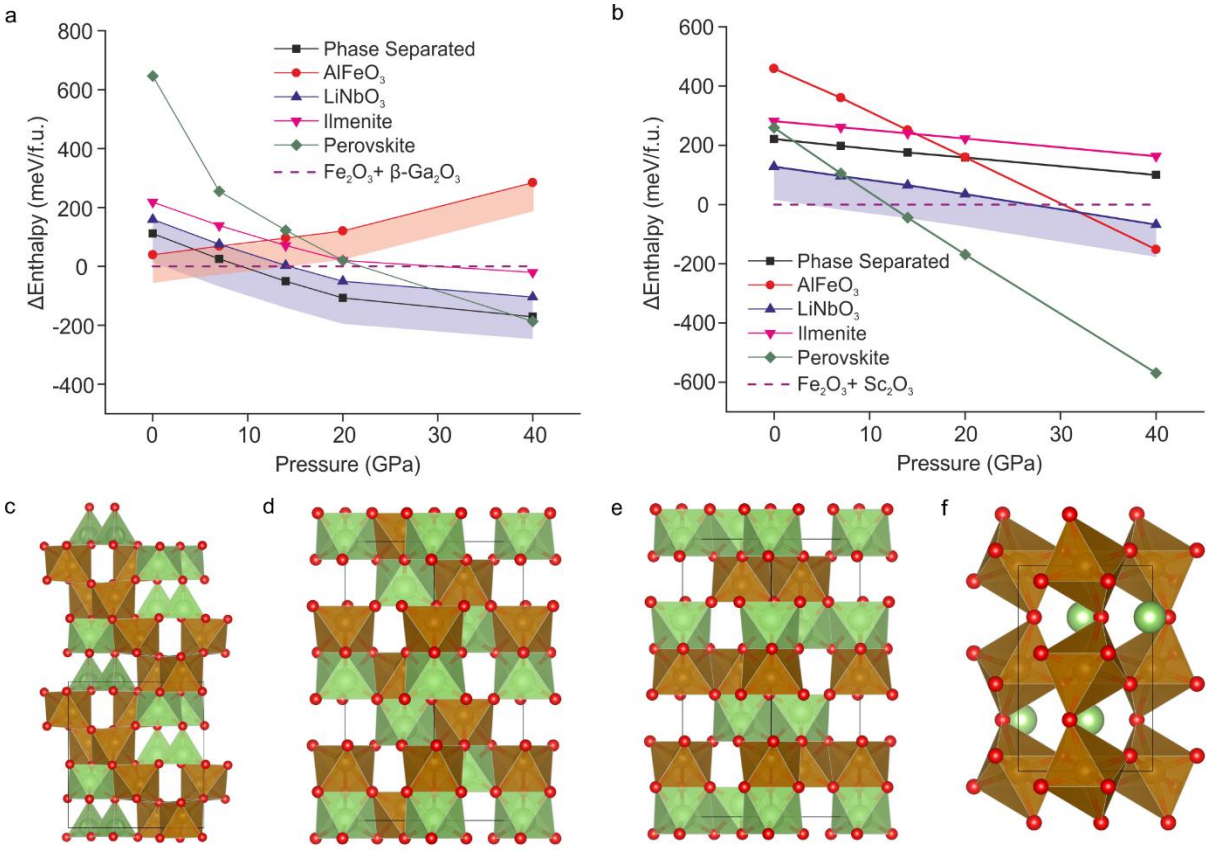

Figure 2: Calculated enthalpies as a function of pressure for (a) $GaFeO_3$ polymorphs in the AFM state, and (b) $ScFeO_3$ polymorphs in the AFM state, plotted relative to the binary oxides α-Fe_2O_3 + β-Ga_2O_3 and α-Fe_2O_3 + Sc_2O_3. The shaded areas represent an estimate of the configurational entropy of $GaFeO_3$ and $ScFeO_3$ at the respective synthesis temperatures of 1200 K and 1800 K: 98.8 meV/f.u. for the ambient pressure $AlFeO_3$-type $GaFeO_3$; 143 meV/f.u. for corundum $GaFeO_3$ and 106 meV/f.u. for corundum $ScFeO_3$. (c) the ambient pressure $AlFeO_3$-type structure of $GaFeO_3$ viewed along [001], which features edge-sharing chains of (Fe, Ga) octahedra parallel to vertex-linked GaO_4 tetrahedra, (d) the polar $LiNbO_3$-type cation ordering in the corundum structure, (e) the non-polar $FeTiO_3$ (ilmenite)-type cation ordering in the corundum structure, (f) the optimised *Pbnm* perovskite-type structure used for this calculation, which represents the phase that is accessible experimentally under applied pressures of 25 GPa[25]. Atom colours: green = Ga(Sc), brown = Fe, red = O.

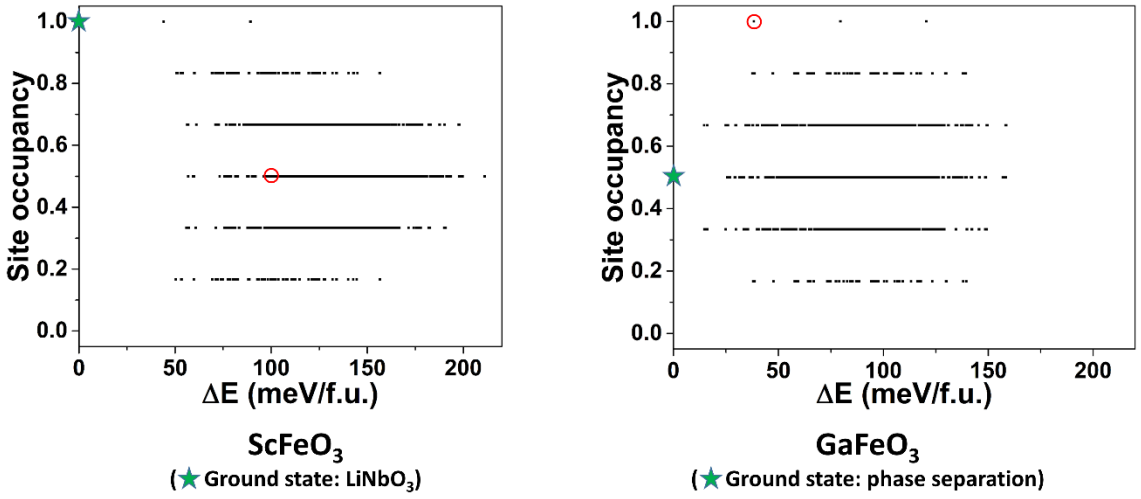

Figure 3: Calculated stabilities of different cation configurations in a hexagonal corundum-type unit cell. Site occupancies (defined as the proportion of Fe^{3+} cations in a given configuration that are coincident with Fe^{3+} positions in the fully ordered $LiNbO_3$ structure) of different configurations are plotted against their relative energies with respect to the ground state of $ScFeO_3$ (left) and $GaFeO_3$ (right). The phase separated structure of $ScFeO_3$ and the $LiNbO_3$-type $GaFeO_3$ are highlighted in red circles. The lowest energy configuration is marked with a green star symbol.

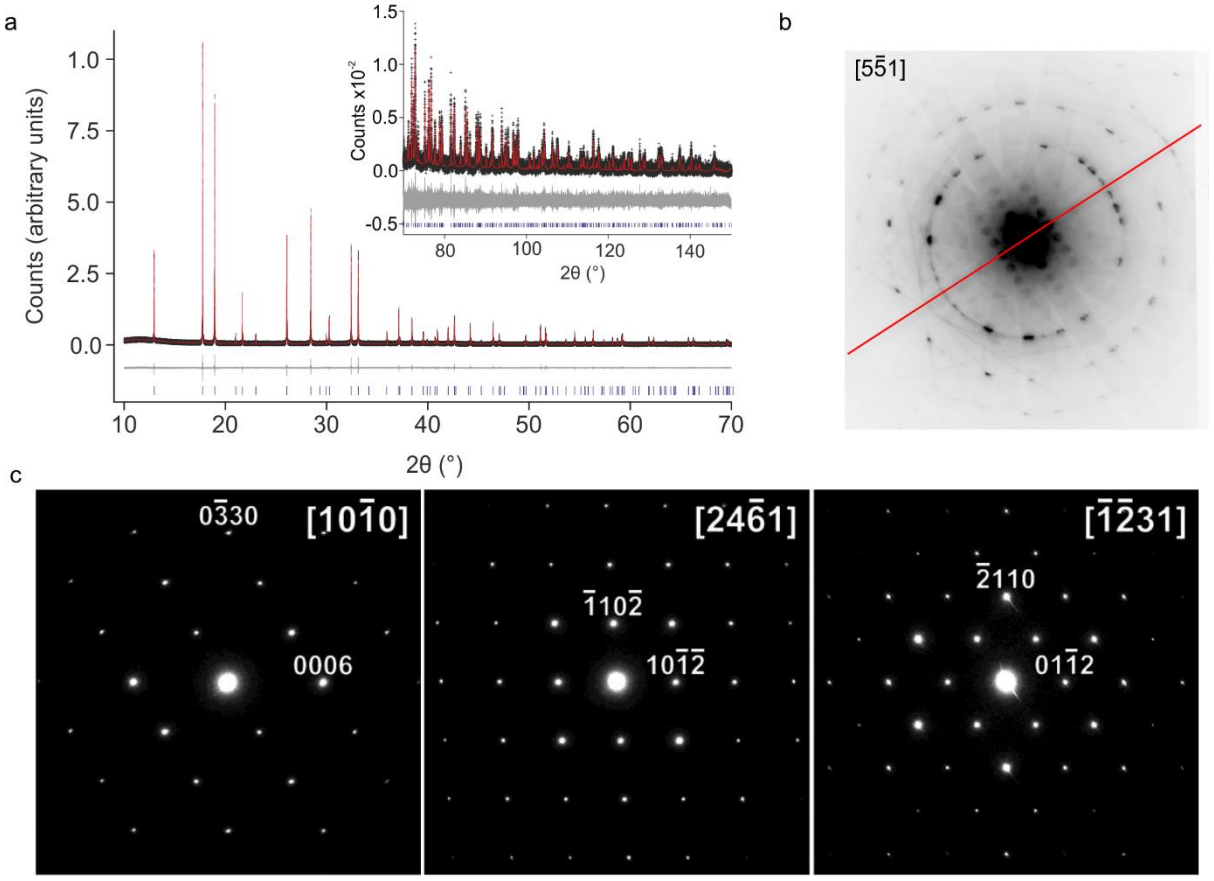

Figure 4: Unit cell and space group determination. (a) LeBail fit to SXRD data (λ = 0.8256185 Å) of corundum $GaFeO_3$ in the hexagonal setting of space group $R\bar{3}c$, which has the highest symmetry consistent with the systematic absences, yields a refined unit cell of dimensions a = 5.01959(3), c = 13.5907(2) Å. The fit to high angle data (70 < 2θ < 150°) is inset. Black markers = y_{obs}, red line = y_{calc}, grey line = y_{obs} - y_{calc}, blue tick marks = allowed *hkl* reflections. (b) CBED [5$\bar{5}$1] zone axis pattern of corundum $GaFeO_3$, which contains a mirror plane as the only symmetry element, consistent with space group *R*3*c*. (c) SAED patterns from three different zone axes, confirming the rhombohedral cell and systematic absences observed by SXRD.

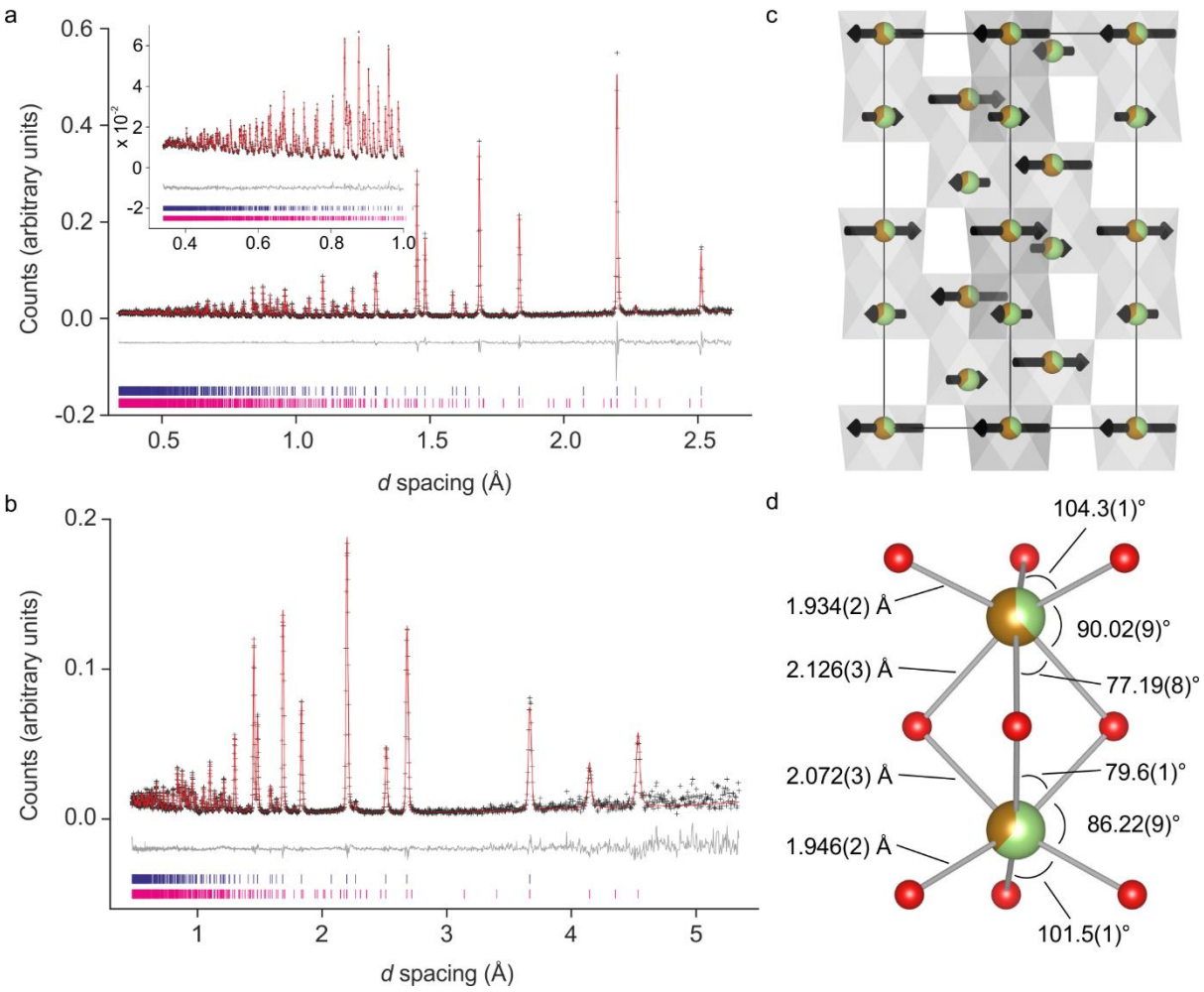

Figure 5: Refined polar corundum structure of $GaFeO_3$. (a) Rietveld refinement against NPD data from the Polaris back-scattering bank (inset: fit to the low *d*-spacing region), and (b) against Polaris bank 3 ($2\theta = 52.2°$), which features two intense peaks of magnetic origin in the range $4 < d < 5$ Å; black markers = y_{obs}, red line = y_{calc}, grey line = $y_{obs} - y_{calc}$, blue tick marks = nuclear structure, magenta tick marks = magnetic structure. (c) The refined nuclear and magnetic structure of $GaFeO_3$ viewed along 110. At each atom, green segments indicate Ga occupancy, brown segments indicate Fe occupancy, black arrows indicate magnetic moments which are ordered parallel to the *a* axis in an antiferromagnetic arrangement. The magnitudes of the ordered moments are indicated by the sizes of the arrows. (d) The local coordination environments of the two crystallographically independent cation sites, which occupy adjacent face-sharing octahedra. The colours indicate the extent of occupancy by Fe (brown) and Ga (green).

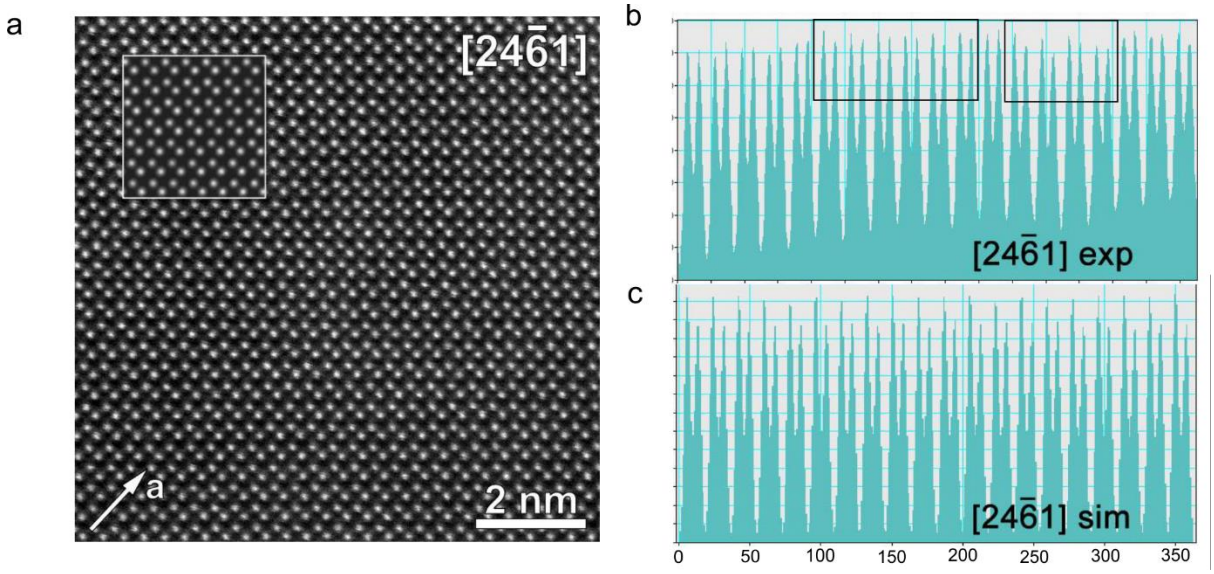

Figure 6: HAADF-STEM analysis of polar corundum $GaFeO_3$ (a) Experimental HAADF-STEM image from the [24$\bar{6}$1] axis, with a simulated image (inset) generated from the refined (PND) crystal structure. (b) Intensity profiles measured from individual rows of atomic columns over large areas from the experimental image, and (c) intensity profiles measured over large areas from the simulated image. Regions in (b) that resemble the simulated structure of (c) are marked with black rectangles.

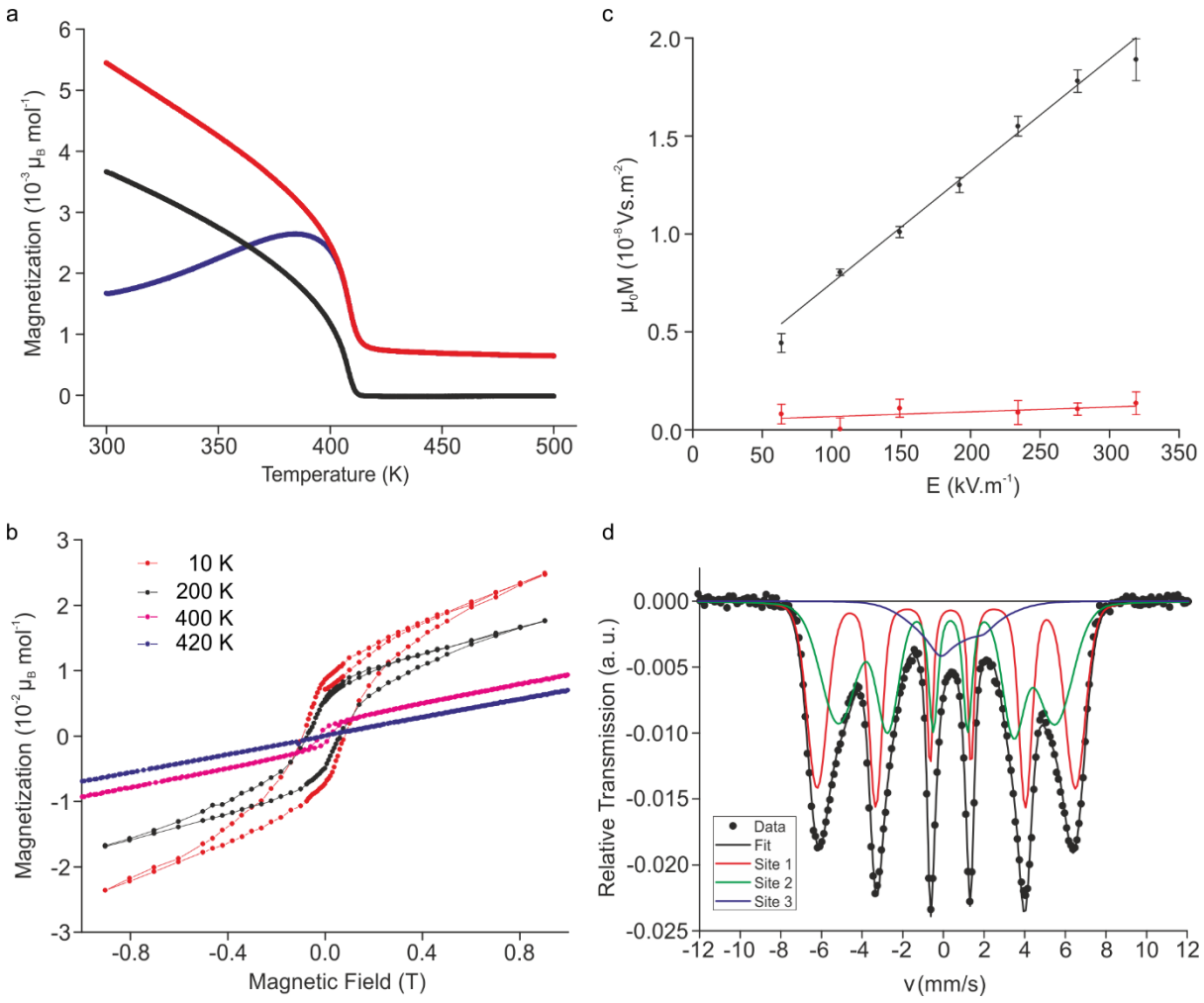

Figure 7. Magnetic properties of polar corundum $GaFeO_3$. (a) Zero-field cooled (blue points), field-cooled (red points) and remanent (black) magnetization as a function of temperature in the range 300 – 500 K, measured with an applied field of 0.1 T. (b) Magnetization as a function of applied magnetic field at temperatures of 10 K (red points), 200 K (black points), 400 K (magenta points) and 420 K (blue points). (c) Induced ac magnetization versus applied ac electric field amplitude at 10 K for two samples: as-made (black points), and post-annealed at 380 °C (red points). (d) ^{57}Fe Mössbauer spectrum at ambient temperature, showing hyperfine splitting consistent with long-range magnetic ordering, and fitted with a three-site model (see Table 3 for fitted parameters).

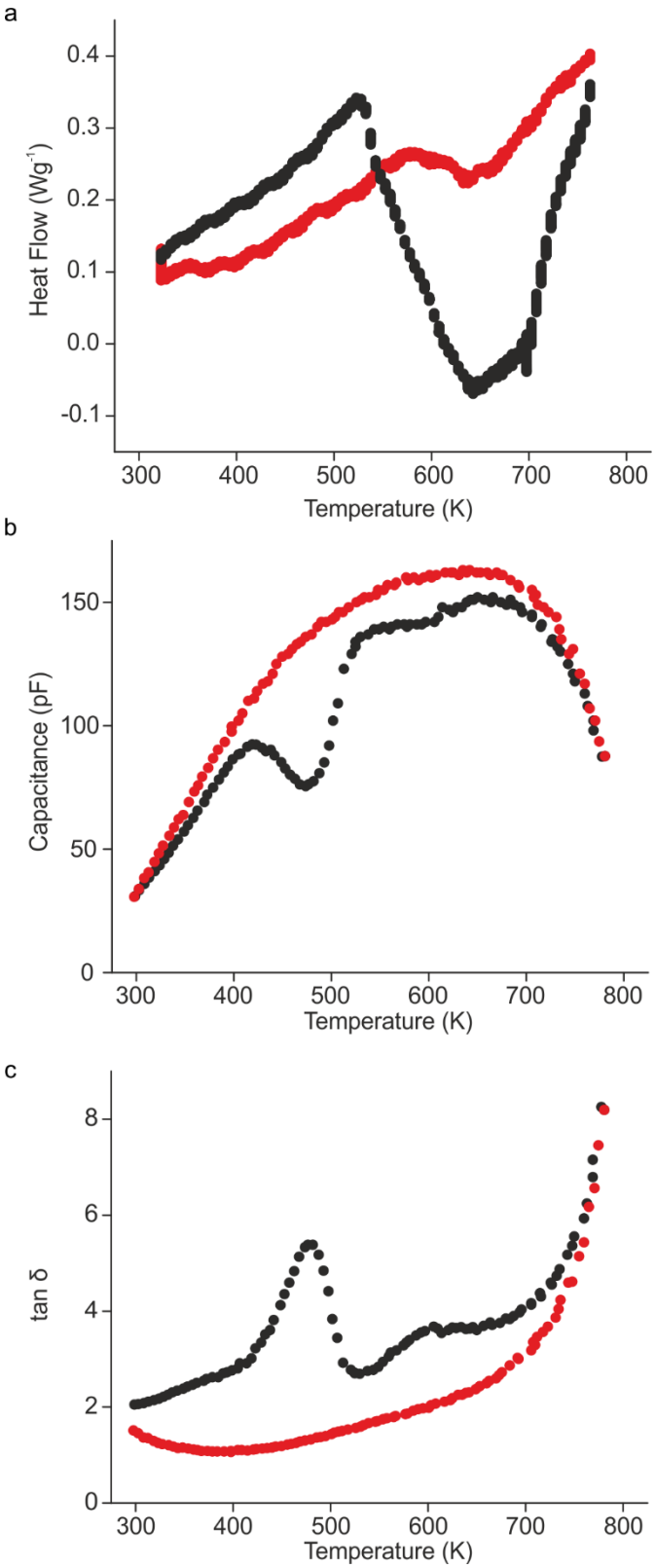

Figure 8: Calorimetric and dielectric behaviour of polar corundum $GaFeO_3$ synthesised at 900 °C. (a) DSC scans performed on heating, black points represent the first cycle and red points represent the second cycle. (b) Capacitance data recorded on first heating cycle (black points) and second heating cycle (red points). (c) Dielectric loss recorded on first heating cycle (black points) and second heating cycle (red points).

Table 1: Structural parameters for *R*3*c* $GaFeO_3$ (sample 1) from Rietveld refinement against room temperature NPD, with refined lattice parameters a = 5.01871(9) Å, c = 13.5879(3) Å, V = 296.39(1) $Å^3$.

	x	y	z	B_{iso} / $Å^2$	Occ.	M / μ_B
Ga(1)	0	0	0	0.231(3)	0.32(2)	
Fe(1)	0	0	0	0.231(3)	0.68(2)	1.03(3)
Fe(2)	0	0	0.28919(5)	0.231(3)	0.32(2)	2.15(2)
Ga(2)	0	0	0.28919(5)	0.231(3)	0.68(2)	
O(1)	0.3026(2)	-0.0046(4)	0.8922(3)	0.284 (5)	1	

Table 2: Structural parameters for *R*3*c* $GaFeO_3$ (sample 2) refined against room temperature NPD data, with refined lattice parameters a = 5.02547(9) Å, c = 13.6057(3) Å, V = 297.31 (2) $Å^3$.

	x	y	z	B_{iso} / $Å^2$	Occ.	M / μ_B
Ga(1)	0	0	0	0.216(4)	0.38(3)	
Fe(1)	0	0	0	0.216(4)	0.62(3)	1.08(4)
Fe(2)	0	0	0.28906(5)	0.216(4)	0.38(3)	2.00(3)
Ga(2)	0	0	0.28906(5)	0.216(4)	0.62(3)	
O(1)	0.3030(3)	-0.0033(5)	0.8916(2)	0.34(2)	1	

Table 3: Mössbauer fitting parameters for the spectrum of Figure 7. The errors are provided in brackets.

Site	B_{hf} (T)	ΔB_{hf} (T)	IS (mm/s)	QS (mm/s)	A (%)
1	39.49(2)	0.28(1)	0.249(3)	0.21(1)	44.00(1)
2	33.11(2)	0.37(1)	0.257(3)	0.19(1)	47.09(1)
3	0	0	0.93(1)	2.16(3)	8.91(1)

Acknowlegements

This work was funded by the EPSRC under EP/N004884. We thank the STFC for provision of beam time at ISIS and Diamond Light Source. We thank the Materials Chemistry Consortium (EPSRC, EP/L000202) for access to computer time on the ARCHER UK National Supercomputing Service (http://www.archer.ac.uk). AMA is grateful to the Russian Science Foundation (grant 14-13-00680) for financial support. MJR is a Royal Society Research Professor.

References

1. Scott, J. F., *Nature Materials* **2007,** *6* (4), 256-257.

2. Bibes, M.; Barthelemy, A., *Nature Materials* **2008,** *7* (6), 425-426.

3. Hill, N. A., *Journal of Physical Chemistry B* **2000,** *104* (29), 6694-6709.

4. Hill, N. A.; Filippetti, A., *Journal of Magnetism and Magnetic Materials* **2002,** *242*, 976-979.

5. Khomskii, D. I., *Journal of Magnetism and Magnetic Materials* **2006,** *306* (1), 1-8.

6. Sando, D.; Barthélémy, A.; Bibes, M., *Journal of Physics: Condensed Matter* **2014,** *26* (47), 473201.

7. Catalan, G.; Scott, J. F., *Advanced Materials* **2009,** *21* (24), 2463-2485.

8. Wang, J.; Neaton, J. B.; Zheng, H.; Nagarajan, V.; Ogale, S. B.; Liu, B.; Viehland, D.; Vaithyanathan, V.; Schlom, D. G.; Waghmare, U. V.; Spaldin, N. A.; Rabe, K. M.; Wuttig, M.; Ramesh, R., *Science* **2003,** *299* (5613), 1719-1722.

9. Heron, J. T.; Trassin, M.; Ashraf, K.; Gajek, M.; He, Q.; Yang, S. Y.; Nikonov, D. E.; Chu, Y. H.; Salahuddin, S.; Ramesh, R., *Physical Review Letters* **2011,** *107* (21).

10. Mandal, P.; Pitcher, M. J.; Alaria, J.; Niu, H.; Borisov, P.; Stamenov, P.; Claridge, J. B.; Rosseinsky, M. J., *Nature* **2015,** *525* (7569), 363-366.

11. Benedek, N. A.; Fennie, C. J., *Physical Review Letters* **2011,** *106* (10).

12. Pitcher, M. J.; Mandal, P.; Dyer, M. S.; Alaria, J.; Borisov, P.; Niu, H.; Claridge, J. B.; Rosseinsky, M. J., *Science* **2015,** *347* (6220), 420-424.

13. Alaria, J.; Borisov, P.; Dyer, M. S.; Manning, T. D.; Lepadatu, S.; Cain, M. G.; Mishina, E. D.; Sherstyuk, N. E.; Ilyin, N. A.; Hadermann, J.; Lederman, D.; Claridge, J. B.; Rosseinsky, M. J., *Chemical Science* **2014,** *5* (4), 1599-1610.

14. Li, M.-R.; Adem, U.; McMitchell, S. R. C.; Xu, Z.; Thomas, C. I.; Warren, J. E.; Giap, D. V.; Niu, H.; Wan, X.; Palgrave, R. G.; Schiffmann, F.; Cora, F.; Slater, B.; Burnett, T. L.; Cain, M. G.; Abakumov, A. M.; van Tendeloo, G.; Thomas, M. F.; Rosseinsky, M. J.; Claridge, J. B., *Journal of the American Chemical Society* **2012,** *134* (8), 3737-3747.

15. Li, M. R.; Walker, D.; Retuerto, M.; Sarkar, T.; Hadermann, J.; Stephens, P. W.; Croft, M.; Ignatov, A.; Grams, C. P.; Hemberger, J.; Nowik, I.; Halasyamani, P. S.; Tran, T. T.; Mukherjee, S.; Dasgupta, T. S.; Greenblatt, M., *Angewandte Chemie-International Edition* **2013,** *52* (32), 8406-8410.

16. Li, M. R.; Stephens, P. W.; Retuerto, M.; Sarkar, T.; Grams, C. P.; Hemberger, J.; Croft, M. C.; Walker, D.; Greenblatt, M., *Journal of the American Chemical Society* **2014,** *136* (24), 8508-8511.

17. Ye, M.; Vanderbilt, D., *Physical Review B* **2016,** *93* (13), 134303.

18. Kawamoto, T.; Fujita, K.; Yamada, I.; Matoba, T.; Kim, S. J.; Gao, P.; Pan, X.; Findlay, S. D.; Tassel, C.; Kageyama, H.; Studer, A. J.; Hester, J.; Irifune, T.; Akamatsu, H.; Tanaka, K., *Journal of the American Chemical Society* **2014,** *136* (43), 15291-15299.

19. Bréard, Y.; Fjellvåg, H.; Hauback, B., *Solid State Communications* **2011,** *151* (3), 223-226.

20. Sharma, K.; Reddy, V. R.; Gupta, A.; Kaushik, S. D.; Siruguri, V., *Journal of Physics-Condensed Matter* **2012,** *24* (37).

21. Uk Kang, K.; Baek Kim, S.; Yong An, S.; Cheong, S.-W.; Sung Kim, C., *Journal of Magnetism and Magnetic Materials* **2006,** *304* (2), e769-e771.

22. O'Dell, T. H., *International Journal of Magnetism* **1973,** *4* (3), 239-244.

23. Arima, T.; Higashiyama, D.; Kaneko, Y.; He, J. P.; Goto, T.; Miyasaka, S.; Kimura, T.; Oikawa, K.; Kamiyama, T.; Kumai, R.; Tokura, Y., *Physical Review B* **2004,** *70* (6), 064426.

24. Fujita, K.; Kawamoto, T.; Yamada, I.; Hernandez, O.; Hayashi, N.; Akamatsu, H.; Lafargue-Dit-Hauret, W.; Rocquefelte, X.; Fukuzumi, M.; Manuel, P.; Studer, A. J.; Knee, C. S.; Tanaka, K., *Chemistry of Materials* **2016,** *28* (18), 6644-6655.

25. Arielly, R.; Xu, W. M.; Greenberg, E.; Rozenberg, G. K.; Pasternak, M. P.; Garbarino, G.; Clark, S.; Jeanloz, R., *Physical Review B* **2011,** *84* (9), 094109.

26. Marezio, M.; Remeika, J. P., *Journal of Chemical Physics* **1967,** *46* (5), 1862-1865.

27. Bull, C. L.; Funnell, N. P.; Tucker, M. G.; Hull, S.; Francis, D. J.; Marshall, W. G., *High Pressure Research* **2016**, 1-19.

28. Klotz, S.; Le Godec, Y.; Straessle, T.; Stuhr, U., *Applied Physics Letters* **2008,** *93* (9).

29. Zha, C.-S.; Mibe, K.; Bassett, W. A.; Tschauner, O.; Mao, H.-K.; Hemley, R. J., *Journal of Applied Physics* **2008,** *103* (5), 054908.

30. Le Godec, Y.; Dove, M. T.; Francis, D. J.; Kohn, S. C.; Marshall, W. G.; Pawley, A. R.; Price, G. D.; Redfern, S. A. T.; Rhodes, N.; Ross, N. L.; Schofield, P. F.; Schooneveld, E.; Syfosse, G.; Tucker, M. G.; Welch, M. D., *Mineralogical Magazine* **2001,** *65* (6), 737-748.

31. Borisov, P.; Hochstrat, A.; Shvartsman, V. V.; Kleemann, W., *Review of Scientific Instruments* **2007,** *78* (10), 106105.

32. VandeVondele, J.; Krack, M.; Mohamed, F.; Parrinello, M.; Chassaing, T.; Hutter, J., *Computer Physics Communications* **2005,** *167* (2), 103-128.

33. Hutter, J.; Iannuzzi, M.; Schiffmann, F.; VandeVondele, J., *Wiley Interdisciplinary Reviews: Computational Molecular Science* **2014,** *4* (1), 15-25.

34. VandeVondele, J.; Hutter, J., *Journal of Chemical Physics* **2007,** *127* (11), 114105-114105.

35. Goedecker, S.; Teter, M.; Hutter, J., *Physical Review B* **1996,** *54* (3), 1703-1710.

36. Krack, M., *Theoretical Chemistry Accounts* **2005,** *114* (1-3), 145-152.

37. Adamo, C.; Barone, V., *Journal of Chemical Physics* **1999,** *110* (13), 6158.

38. Ernzerhof, M.; Scuseria, G. E., *Journal of Chemical Physics* **1999,** *110* (11), 5029.

39. Guidon, M.; Hutter, J.; VandeVondele, J., *Journal of Chemical Theory and Computation* **2010,** *6* (8), 2348-2364.

40. Spencer, J.; Alavi, A., *Physical Review B* **2008,** *77* (19), 193110-193110.

41. Pauling, L.; Hendricks, S. B., *Journal of the American Chemical Society* **1925,** *47*, 781-790.

42. Blake, R. L.; Hessevick, R. E.; Zoltai, T.; Finger, L. W., *American Mineralogist* **1966,** *51* (1-2), 123-129.

43. Buxton, B. F.; Eades, J. A.; Steeds, J. W.; Rackham, G. M., *Philos. Trans. R. Soc. A-Math. Phys. Eng. Sci.* **1976,** *281* (1301), 171-194.

44. Wills, A. S., *Physica B* **2000,** *276*, 680-681.

45. Shull, C. G.; Strauser, W. A.; Wollan, E. O., *Physical Review* **1951,** *83* (2), 333-345.

46. Capillas, C.; Tasci, E. S.; de la Flor, G.; Orobengoa, D.; Perez-Mato, J. M.; Aroyo, M. I., *Zeitschrift Fur Kristallographie* **2011,** *226* (2), 186-196.

47. Murad, E., *American Mineralogist* **1982,** *67* (9-10), 1007-1011.

48. Forsyth, J. B.; Hedley, I. G.; Johnson, C. E., *Journal of Physics Part C Solid State Physics* **1968,** *1* (1), 179-188.

49. Schmid, H., *Journal of Physics-Condensed Matter* **2008,** *20* (43).

50. Perez-Mato, J. M.; Gallego, S. V.; Tasci, E. S.; Elcoro, L.; de la Flor, G.; Aroyo, M. I., Symmetry-Based Computational Tools for Magnetic Crystallography. In *Annual Review of Materials Research, Vol 45*, Clarke, D. R., Ed. 2015; Vol. 45, pp 217-248.

51. Mandal, P.; Pitcher, M. J.; Alaria, J.; Niu, H. J.; Zanella, M.; Claridge, J. B.; Rosseinsky, M. J., *Advanced Functional Materials* **2016,** *26* (15), 2523-2531.

52. Mohamed, M. B.; Senyshyn, A.; Ehrenberg, H.; Fuess, H., *Journal of Alloys and Compounds* **2010,** *492* (1–2), L20-L27.

1

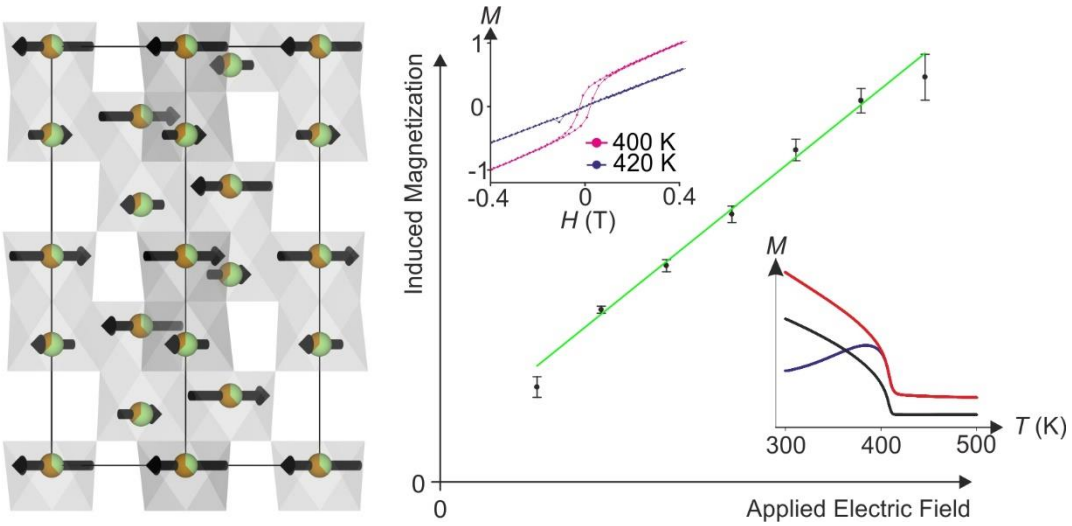
M
1
0
-1
-0.4
0
0.4
H (T)
400 K
420 K
Induced Magnetization
M
300
400
500
T (K)
0
0
Applied Electric Field